

Automatic vocal tract landmark localization from midsagittal MRI data

Mohammad Eslami, Christiane Neuschaefer-Rube, Antoine Serrurier
 Clinic for Phoniatrics, Pedaudiology & Communication Disorders,
 University Hospital and Medical Faculty
 RWTH Aachen University, Germany

Abstract—The various speech sounds of a language are obtained by varying the shape and position of the articulators surrounding the vocal tract. Analyzing their variability is crucial for understanding speech production, diagnosing speech and swallowing disorders and building intuitive applications for rehabilitation. Magnetic Resonance Imaging (MRI) is currently the most harmless powerful imaging modality used for this purpose. Identifying key anatomical landmarks on it is a pre-requisite for further analyses. This is a challenging task considering the high inter- and intra-speaker variability and the mutual interaction between the articulators. This study intends to solve this issue automatically for the first time. For this purpose, midsagittal anatomical MRI for 9 speakers sustaining 62 articulations and annotated with the location of 21 key anatomical landmarks are considered. Four state-of-the-art methods, including deep learning methods, are adapted from the literature for facial landmark localization and human pose estimation and evaluated. Furthermore, an approach based on the description of each landmark location as a heat-map image stored in a channel of a single multi-channel image embedding all landmarks is proposed. The generation of such a multi-channel image from an input MRI image is tested through two deep learning networks, one taken from the literature and one designed on purpose in this study, the *flat-net*. Results show that the *flat-net* approach outperforms the other methods, leading to an overall Root Mean Square Error of 3.4 pixels/0.34 cm obtained in a leave-one-out procedure over the speakers. All of the codes are publicly available on GitHub.

Index Terms—landmark localization, landmark detection, key-point localization, MRI, speech, vocal tract, deep learning

I. INTRODUCTION

In speech production, the sounds of a language are obtained by varying the shape and position of the organs surrounding the vocal tract. This region is characterized by a high inter- and intra-speaker articulatory variability, both in the space and time domains. Analyzing and modeling the shape of the vocal tract articulators is therefore crucial for speech production research [1]–[3] and for diagnosis and therapy of related disorders, including speech disorders [4], [5], velopharyngeal insufficiency [6] and swallowing dysfunctions [7]. The vocal tract extends from the glottis to the lips and comprises various structures such as the larynx, the epiglottis, the velum, the tongue, and the upper and lower lips. Modeling their variability necessitates as pre-requisite to be able to identify the same anatomical features on these structures across speakers and articulations. One way of achieving this is to determine on each articulation the same key anatomical landmarks characterizing these structures or demarcating them.

Articulatory speech production studies often rely on midsagittal images of the vocal tract and Magnetic Resonance Imaging (MRI) constitutes in this approach an essential modality [8]–[10]. This study focuses therefore on the localization of anatomical landmarks of the vocal tract on midsagittal MRI. Nowadays, landmarks are labelled manually on MRI data [3], [11]. However, the increasing number of data [12] and the recent progress in data science call for an automatic approach. To our knowledge, this is the first study to consider and solve this issue automatically.

Localizing anatomical landmarks on images, sometimes referred to as detecting keypoints, has already been considered for various structures in the biomedical field. This is for instance the case for the aortic valve [13], the lumbar spine [14] and the craniomaxillofacial region [15]. It has also been considered as part of more global registration processes, such as for the eye between fundus photographs and MRI [16] or for the liver between the computed tomography images of various phases [17]. It has also been used for instance to identify regions of interest, such as for the brain for Alzheimer’s disease diagnosis [18], [19].

These applications take place in a more general framework in computer vision where localizing automatically landmarks on images is a long-standing problem. Two fields of application in this context appear more particularly connected to our problem. The first is the localization of landmarks for the face, for which a comprehensive review is provided by Wu *et al.* [20]. Facial landmark detection represents a challenging issue due to the high variability of the shapes, poses, occlusions, and lighting conditions. A current challenge is the detection of the 68 landmarks specified in the 300W dataset [21]. Similarly, localizing the position of the joints of the body on images to estimate the human pose is also a long-standing problem [22]. It is also a challenging issue in computer vision due to the high variability of the postures, body shapes, actions, clothes and scenes. A current challenge is the detection of the 16 body joint positions specified in the *MPII Human Pose* dataset [23]. These problems constitute the closest problems found in the literature related to our issue and actively studied. The solutions proposed in this study are inspired by this literature.

One of the state-of-the-art methods to localize facial landmarks relies on regressions implemented in a boosting approach, the *dlib* method [24]. The majority of the recent techniques rely however on deep learning (DL) neural networks,

known to be powerful to automatically identify and combine key features from input data to solve the considered problem. Notable current methods for facial landmark estimation include the so-called *deep alignment network* [25] and the *HyperFace* method [26]. For human pose estimation, a recent method is the *multi-context attention model* [27], an extension of the *stacked hourglass networks* [28]. The architecture of the networks used in these methods are based on Convolutional Neural Networks (CNNs), particularly adapted to the processing of images.

The goal of this study is to investigate and propose fully-automated end-to-end image analysis methods for localizing key anatomical landmarks of the vocal tract from midsagittal MRI data. It is aimed to be used in the future for new speakers for which no prior data are available. For this purpose, the *dlib* method as well as the three methods based on DL mentioned above, all designed for the localization of landmarks/joints on images, will be adapted to our problem and evaluated. In addition, in an attempt to increase the accuracy, a dedicated method specifically designed for the localization of vocal tract landmarks on midsagittal MRI will be proposed. This method aims at describing each single landmark as a full image with a maximal intensity on the landmark localization, referred to as a *heat-map*. Several landmarks can be described as several output channels, leading to the concept of *heat-maps in channels*. The localization of landmarks consists therefore in generating *heat-maps in channels* from input MRI images. Two DL networks will be tested for the generation of such heat-maps: (1) the generator network of the *pix2pix* method [29], known to be efficient to generate images as in our problem, and (2) a dedicated network developed on purpose in this study.

No benchmark exists for the problem described in this study and datasets in the field of articulatory speech analyses are usually rather limited and characterized by high shape and noise variability [3]. The dataset considered for this study is in agreement with this remark and therefore much more limited and heterogeneous than the datasets mentioned above for facial landmark localization and human pose estimation, increasing the challenge. The code for the six methods considered and evaluated in this study is shared publicly for research and validation purposes.

The rest of the paper is organized as follows: in section II, the dataset, the anatomical landmarks, the methods, and the evaluation schemes are presented; the section III reports the experimental results, expresses the discussions and future works; finally, the paper is concluded in section IV.

II. MATERIAL AND METHODS

A. Data

The study considers static midsagittal MRI recorded between 2002 and 2011 from 9 French speakers (5 males, 4 females), referred to as *subjects* in this study, sustaining 62 articulations, also referred to as *classes* in the context of machine learning, designed to be representative of the French phonemic repertoire [3], [30]. The images have been recorded either on a 1.5 or on a 3 Tesla MRI scanner and have a field

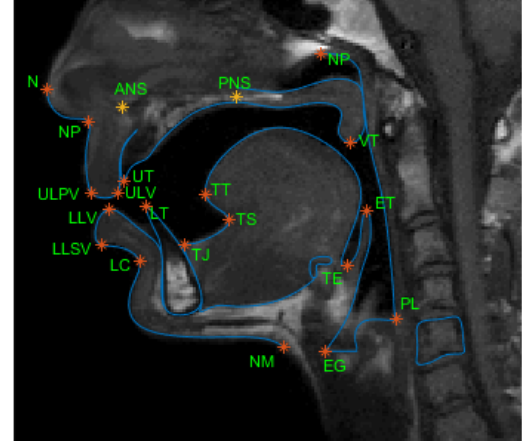


Fig. 1: (Color online) MRI superimposed with the 21 anatomy landmarks of the study.

of view of $256 \times 256 \text{ mm}^2$ and a resolution of 1 mm per pixel. Note that two speakers have been discarded in comparison to [3], [30] due to the significantly lower quality of the images, the different fields of view and the different sizes of the images.

21 anatomical landmarks relevant to the study of the speech articulations have been identified. They represent either characteristic landmarks of the speech articulators, such as the tip of the tongue, or the junction between two articulators. They are listed in Table I and illustrated for one articulation of one subject in Fig. 1. They have been manually identified on all images of the dataset by an expert. Note that the upper and lower teeth landmarks (UT and LT) denote bony structures and, as such, are not distinguishable from the air on MRI data. They have been determined for each subject by contrast with soft tissues on an articulation acquired on purpose and reported on the other images using their relative position with the hard palate. Please refer to [3] for further information regarding this procedure as well as the data collection and processing.

B. Challenges

Localizing landmarks of the vocal tract area on midsagittal MRI images presents particular characteristics. The main challenges are summarized in the following list. Fig. 2 shows a few articulations from different subjects illustrating the diversity of the dataset.

- The shapes and positions of the vocal tract articulators are characterized by a high variability, due to the variety of the speech task and to the different morphologies and articulatory strategies of the speakers to perform a same task.
- Some articulators such as the tongue, velum, lips and epiglottis present a high variability in the vocal tract area, leading to very different locations in the dataset associated to the landmarks VT, TT, TS, LLSV, ULPV, ET and TE.
- Some tissues may touch each others for certain articulations, leading to hardly distinguishable landmarks at these locations, such as TE, TS and ET.

TABLE I: List of the landmarks of interest for vocal tract MRI image analysis.

Abbreviation	Name	Description
TJ	Tongue-Jaw	Junction between the tongue and the jaw
TS	Tongue Sub	Most posterior point of the sublingual cavity
TT	Tongue Tip	Tip of the tongue
TE	Tongue-Epiglottis	Junction between the tongue and the epiglottis
N	Nose	Most anterior point of the tip of the nose
NP	Nose-Philtrum	Junction between the philtrum and the external nose
ULPV	Upper Lip Philtrum Vermillion	Vermillon border of the upper lip
ULV	Upper Lip Vermillion	Junction between the wet and dry vermillion of the upper lip
NM	Neck-Mandible	Junction between the rather horizontal submandibular line and rather vertical neck line
LC	Lip-Chin	Labiomental groove
LLSV	Lower Lip Skin Vermillion	Vermillon border of the lower lip
LLV	Lower Lip Vermillion	Junction between the wet and dry vermillion of the lower lip
LT	Lower Teeth	Upper point of the lower incisors
UT	Upper Teeth	Lower point of the upper incisors
ET	Epiglottis Tip	Tip of the epiglottis
EG	Epiglottis-Glottis	Junction between the epiglottis and the glottis
ANS	Anterior Nasal Spine	Anterior nasal spine
PNS	Posterior Nasal Spine	Posterior nasal spine
VT	Velum Tip	Tip of the velum
PL	Pharynx-Larynx	Junction between the pharyngeal wall and the posterior supraglottic region
NP	Nasopharynx	Upper point of the nasopharynx

- The larynx area appears very difficult to capture on midsagittal MRI data, leading to a confusing area on the images and hardly identifiable landmarks, such as PL and EG.
- Some articulators may occasionally show very different shapes than in the large majority of the articulations, such as the velum rolled up against the tongue for a few articulations [30], leading to unusual location of the landmark VT.
- Two important landmarks for speech production analyses are the teeth landmarks UT and LT, which are not directly visible on the images, as mentioned earlier.
- The images are recorded at different times with different scanners, leading to variable quality and noise levels. Similarly, the quality and noise level may not be homogeneous within a single image.
- Despite the high variability, the size of the available dataset, *i.e.* 9 subjects with 62 articulations, hence 558 articulations, is rather limited in comparison to those usually used for landmark localization in the literature, *e.g.* over 10K images for [23], [26], [31].

C. Methods

Six different methods are compared. Four are state-of-the-art methods taken from the literature (detection of 68 facial landmarks or 16 body joints) and adapted to the current problem and two methods are dedicated methods introduced in this paper. The four methods taken from the literature are the following:

1) *dlib*: The algorithm available as part of the *dlib* library is an implementation of the ensemble of regression trees presented in 2014 by Kazemi and Sullivan [24]. This technique takes advantage of simple features with fast computing capacities, *e.g.* the pixels' intensity differences, to directly estimate the landmark locations. These locations are subsequently refined with an iterative process made of a cascade of regressors

and using gradient boosting. Note that the *dlib* method is the only method considered in this study not based on DL.

2) *HyperFace*: The *HyperFace* method makes use of an end-to-end DL network for simultaneous face detection, landmark localization, pose estimation and gender recognition [26]. It exploits the intermediate layers of a deep CNN, such as the *ResNet-101* [32], by connecting together the intermediate feature maps to further predict the various desired outputs. The last layers of the *HyperFace* network are fully connected layers.

3) *Deep Alignment Network*: The *Deep Alignment Network (DAN)* is a method based on a DL to localize facial landmarks [25]. It consists of multiple stages of CNNs, where each stage improves the locations of the facial landmarks estimated by the previous stage. A key element of the system is the use of heat-maps within each stage. In their approach, a heat-map is defined as an image with highest intensity values at the exact locations of all the considered landmarks and decreasing intensities around as a function of the distance to the nearest landmark. The last two layers of each stage are fully connected layers.

4) *Multi-Context Attention Model*: The *Multi-Context Attention Model (MCAM)* method is an extended version of the DL *stacked hourglass networks* [28] designed for human pose estimation and body joint localization [27]. It generates heat-maps describing the body joint locations by using multiple resolutions, conditional random fields and an original layer type combining various convolutional layers together. For training, the ground truth heat-maps are generated by 2-D Gaussians centered on the joint locations. The generated heat-maps contain all joint locations together and are further split into partial heat-maps for each body joint by means of an extra spatial classifier. Since the network is designed to localize 16 body joints, two of these networks are necessary in practise in the current study to localize the 21 landmarks.

In order to increase the accuracy of the vocal tract landmark localization, two alternative methods more closely designed



Fig. 2: Five images of the database illustrating the variability.

for the specific problem of this study are proposed. These two methods exploit the concept of *heat-maps in channels* and are implemented on two different DL networks, one designed on purpose for this study and the other taken from the literature.

In this approach, each single landmark is described as a full image, the *heat-map*, with a maximal intensity on the landmark location. Several landmarks are described as several channels of an image, the *heat-maps in channels*. Localizing the landmarks on an image consists therefore in generating the associated *heat-maps in channels*, instead of the vectors of the landmarks' locations or one heat-map containing all landmarks as for the previous studies. The landmark locations are then straightforwardly derived from the *heat-maps in channels* as the points with maximal intensity in each channel. Note that this concept of heat-map is related to the concept of heat-maps mentioned in the *DAN* and *MCAM* methods. However, in these methods, the heat-maps contain all landmark/joint locations together and are not directly provided as output of the networks.

Practically, for an input image of size $N \times N$, the network generates L output heat-map images (*i.e.* tensor $H \in R^{N \times N \times L}$) where the l^{th} heat-map ($H_l \in R^{N \times N \times 1}$) has the maximum intensity value at the location of the estimated l^{th} landmark. The normalized target heat-maps are obtained via a Gaussian hat with $\sigma = 10$ pixels and a maximum of 1 around each landmark location. Fig. 3 shows an example of the combination of 3 heat-maps created for 3 landmarks and displayed as the 3 channels of a single RGB image. The predicted location of the l^{th} landmark corresponds to the location of the maximum value in the l^{th} predicted heat-map:

$$(x_p, y_p)_l = \underset{x, y}{\operatorname{argmax}} H_l(x, y), \quad l = 1, \dots, L \quad (1)$$

Two different networks are considered in this study to generate the *heat-maps in channels* : (1) the *flat-net* network, designed on purpose, and (2) the *generator network of the pix2pix* algorithm [29], extracted from the literature and adapted to the current needs. In our approach, the output of the networks are directly the heat-maps, *i.e.* images. For this reason, the fully connected layers found in the *HyperFace* and *DAN* networks, transforming feature maps into landmark location vectors for output, can be omitted.

a) flat-net network: The *flat-net* architecture is presented in Fig. 4. As indicated by its name, it does not contain any pooling, down and up sampling nor fully connected layers but considers various kernel sizes and dilation rates. It is designed

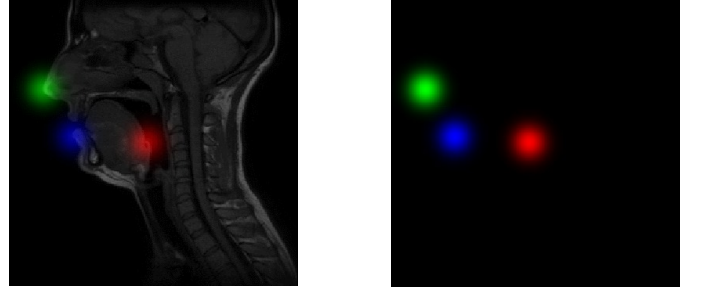


Fig. 3: (Color online) Superposition of 3 heat-maps for 3 different landmarks, represented as the 3 channels of a single RGB image (right), and superimposed on the corresponding input MRI image (left).

to explore in the first layers the image at different resolutions, so as to deal with the different morphologies, and combine the resulting feature maps in a second step to output the desired heat-maps. In layers L1 and L2, convolutional filters of kernel size 9×9 are applied consecutively using 5 different dilation rates. The generated feature maps are then concatenated in layer L3. It is followed by a convolutional layer of kernel size 5×5 and three consecutive convolutional layers of kernel size 1×1 . The activation functions for all convolutional layers are *Relu*, except the last layer (L7) using *tanh*. The number of filters used for each layer is indicated in the Fig. 4. The loss is measured as the mean absolute error between the predicted and the desired heat-maps. Since there is no pooling in this architecture, the concatenation of the layer L3 leads to a very large size tensor, causing practical memory issues. To solve this problem, the prediction of the 21 heat-maps are split in practise into 5 different networks. The additional number of weights resulting from the use of 5 networks in this approach is discussed in section III.

b) pix2pix's generator network: This architecture exploits the generator component of the pix2pix network [29], referred to in the following as *p2p-GN*, standing for *pix2pix's generator network*. It is based on a hourglass-shaped CNN with skip connections. This network is specifically designed to analyze and generate images, hence particularly adapted in our case for the generation of heat-maps from MRI. It has already proved to be very efficient for such tasks [33]. The loss function as well as the hyper-parameters used in this study are those reported by [29]. Experimental analyses showed that this network produces better results when it does not generate more

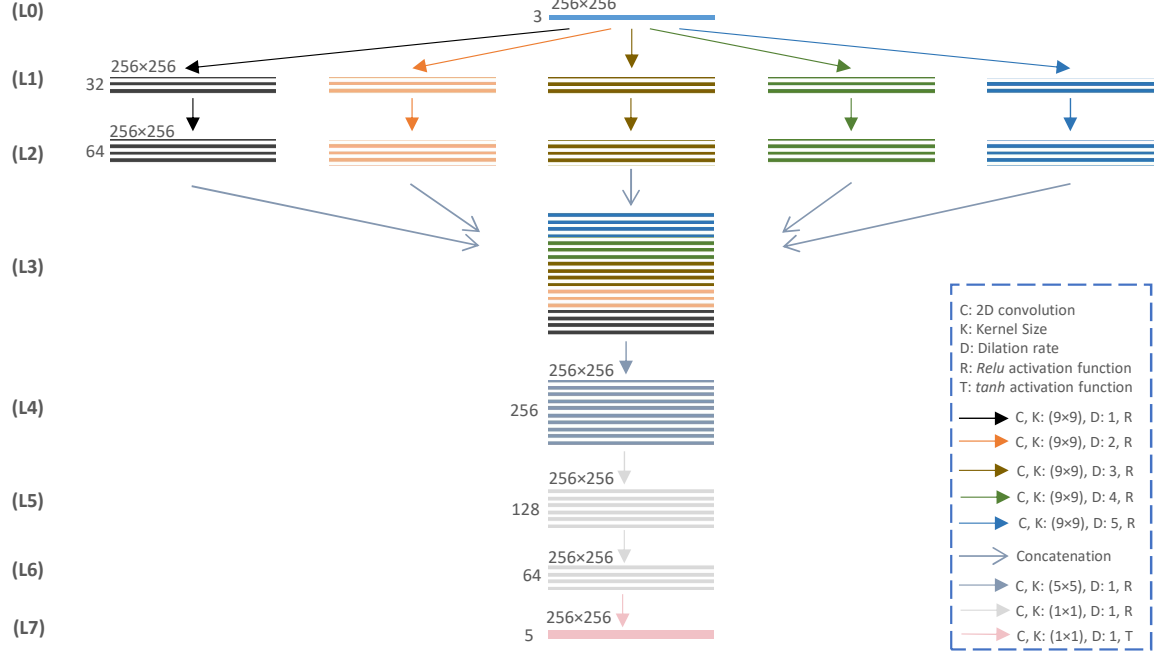


Fig. 4: (Color online) Architecture of one of the *flat-net* networks producing 5 heat-maps corresponding to 5 landmarks.

than 3 heat-maps at the same time. For this reason, similarly to the *flat-net* approach, the prediction of the 21 heat-maps are split into 7 different networks. Again, the additional number of weights resulting from the use of 7 networks in this approach is discussed in section III.

D. Implementation and Evaluation

The 9×62 input grayscale images are converted into grayscale RGB by simple channel repetition to comply with the input format of the networks. Considering the relatively limited number of data, the dataset is augmented [34] via 10 different arbitrary methods as follows: (1) Addition of a Gaussian intensity noise of mean equal to 0 and variance to 12.75, (2) Blurring with a Gaussian of variance $\sigma=5$ pixels, (3-4) Rotation of +10 and -5 degrees, (5-6) Translation of (+30,+10) pixels and (+40,-10) pixels, (7) Rotation of -5 degrees followed translation of (+30,+10) pixels, (8) Zooming out of scale 0.8, (9) Translation of (+30,+10) pixels followed by zooming in of scale 1.2, and (10) Translation of (+40,+20) pixels followed by zooming out of scale 0.9 plus blurring with a Gaussian of variance $\sigma=3$ pixels. By this method, the dataset is artificially augmented from $9 \times 62 = 558$ to $11 \times 9 \times 62 = 6138$ images.

The errors of prediction of the landmark coordinates are evaluated by means of Euclidean distance and Root Mean Squared Error (RMSE). The Euclidean distances are expressed in pixels to comply with the existing results in the literature of the domain while the RMSE is expressed in centimeters to provide comprehensive and interpretable results for speech analyses purposes.

For the l^{th} landmark, if $(x_g, y_g)_l$ and $(x_p, y_p)_l$ denote respectively the ground-truth and the predicted coordinates,

the Euclidean distance d_l is calculated as follows:

$$d_l = \sqrt{(x_g - x_p)_l^2 + (y_g - y_p)_l^2} \quad (2)$$

Using similar notations, the RMSE is calculated as follows:

$$RMSE = \sqrt{\frac{1}{Q} \sum_{q=1}^Q (x_g - x_p)_q^2 + (y_g - y_p)_q^2} \quad (3)$$

where Q is the number of considered elements, *e.g.* all the landmarks of all images, and q is the corresponding index.

Most of the landmark localization methods are evaluated in the literature by a hold-out scheme, *i.e.* by splitting the data into train/test sets, for instance 21,997/1,000 for the *HyperFace* method [26], 2,000/330 for the *dlib* method [24] or 3148/600 for the *DAN* method [25]. In the current application, the ultimate objective is however to localize landmarks on new speakers, *i.e.* on speakers where no data were available before. To comply both with the literature benchmarks and the specificity of the study, the performances are evaluated via two schemes: (1) the randomized 10-fold cross-validation (CV) and (2) the leave-one-subject-out cross-validation (LoSo). Note in addition that 5% of the training data in each session are randomly set aside in advance for validation purposes and tracking the learning curves.

In the CV scheme, the augmented dataset is randomly split into 10 groups, 9 being used for training purposes, *i.e.* 5,525 samples, and 1 for test purposes, *i.e.* 613 samples. The training and evaluation is then repeated 10 times until each single group has been used as the test set. Each sample is therefore being used as a test sample at some point during the process. Note that in this evaluation scheme, the train and test sets may share data of same subjects and/or of same articulations, making the two sets not completely independent. However, in accordance

with the literature in the domain, a very large dataset with many more subjects and articulations could be perfectly evaluated through this scheme and is therefore considered in this study. Above all, this scheme is considered in our evaluation to assess the validity of the hyper-parameters reported by the methods for our environment.

In the LoSo scheme, the 62 images of one arbitrary subject are set aside to serve as the test set. The remaining images are then augmented, leading to $8 \times 62 \times 11 = 5,456$ images, and used for the training. In other words, the network is not trained with data from the test subject. The training and evaluation is then repeated 9 times until each subject has been used as the test set. Each sample is therefore being used as a test sample at some point during the process on a model trained on the other subjects. This scheme is much stricter and challenging than the CV scheme as the trained network does not contain any information regarding the tested subject. Note however that the train and test sets may still share data of same articulations. This point will be revisited in the discussion.

The results for the two evaluation schemes are presented in the section III. All of the hyper-parameters of the methods taken from the literature are set to their default values mentioned in their corresponding studies. The training machine was made of an Intel Xeon w-2145 (3.70 GHz) CPU and a NVIDIA Tesla P100-SXM2-16GB GPU. Except for *dlib*, all the methods are trained on GPU. All the implementation are available online on GitHub¹.

III. RESULTS AND DISCUSSION

A. Results

An overall comparison of the performances of the six methods are provided in Fig. 5 for both the CV and the LoSo schemes. It displays in box plots the Euclidean distances between the predicted and true landmark locations. For each box, the central mark indicates the median while the bottom and top edges indicate respectively the 25th and 75th percentiles. The whiskers extend to the most extreme data points not considered as outliers, the outliers being plotted individually using the ‘+’ symbol. A detail of these results per landmark is provided in Figs. 6 and 7 for the CV and the LoSo schemes respectively.

Regarding the CV scheme, all the methods show good accuracy, with boxes below 2.5 pixels, except the *MCAM* method. This might be ascribed to the design of the method, optimized for joint localization and not anatomical landmarks as in the current case. Nevertheless, the method still shows decent results, with 75% of the distance errors being smaller than 5 pixels. On the other side, the *dlib* method presents the best results, possibly due to its boosting approach. The errors appear rather equally distributed between landmarks, the highest error being observed for EG regardless of the method.

By attempting to predict landmarks on a subject not used to train the models, the LoSo evaluation scheme is more constraining and presents logically deteriorated – but more pertinent – results in comparison to the CV evaluation scheme. The results for the *DAN*, *MCAM* and *HyperFace* methods

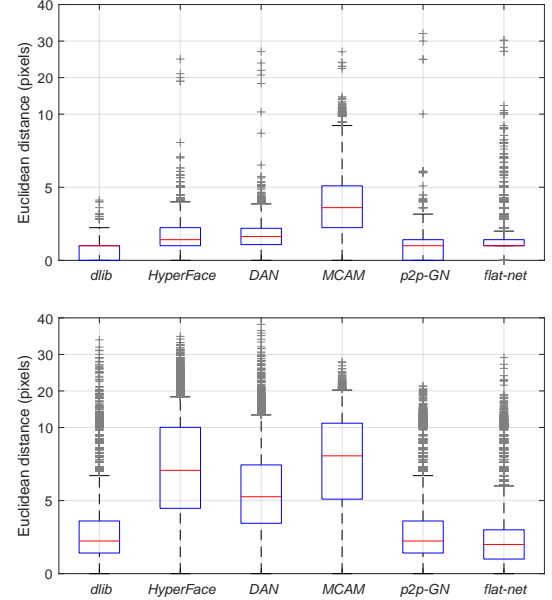


Fig. 5: Box plots of the overall Euclidean distances between the predicted and true landmark locations for the 6 methods of the study, for the CV (top) and LoSo (bottom) evaluation schemes. Note the y-axis scale, linear in two steps to zoom in the 0-10 pixels range.

appear in particular significantly deteriorated. On the contrary, the deterioration appears more limited for the three other methods. The best results are achieved for the *flat-net* architecture, while the *p2p-GN* architecture and the *dlib* method still lead to fairly good accuracy, with boxes remaining below 3.5 pixels. As in the CV scheme, the highest errors are observed for the landmark EG, followed in this scheme by VT and NM.

The learning curves for the five networks of the study are displayed in Fig. 8. As visible, all the methods for both schemes converge without much difference between the train and validation sets. Note that the learning curves cannot be compared across methods due to the differences in the loss functions, in the optimizers and in the hyper-parameters.

The results in terms of RMSE are provided in Fig. 9. It confirms the lower accuracy already noted for the LoSo scheme in comparison to the CV scheme. It also shows that the three methods *HyperFace*, *DAN* and *MCAM* estimate in the LoSo scheme many landmarks for more than 50% of the images with an error larger than 0.5 cm (5 pixels), rather problematic for speech production studies. On the contrary, the three methods *dlib*, *p2p-GN* and *flat-net* still show acceptable results, with almost all landmarks for more than 70% of the images having an error lower than 0.5 cm. It means that the three first methods are not suitable to handle satisfactorily the data and problem presented in this study. A larger dataset with significantly more subjects and articulations might solve this issue. On the contrary, the three latter methods provide fairly good results in the LoSo scheme despite the limited dataset. The figure confirms also that the worst results are achieved for the EG, NM and VT landmarks in the LoSo scheme.

A summary of the results and characteristics of the six

¹<https://github.com/mohaEs>

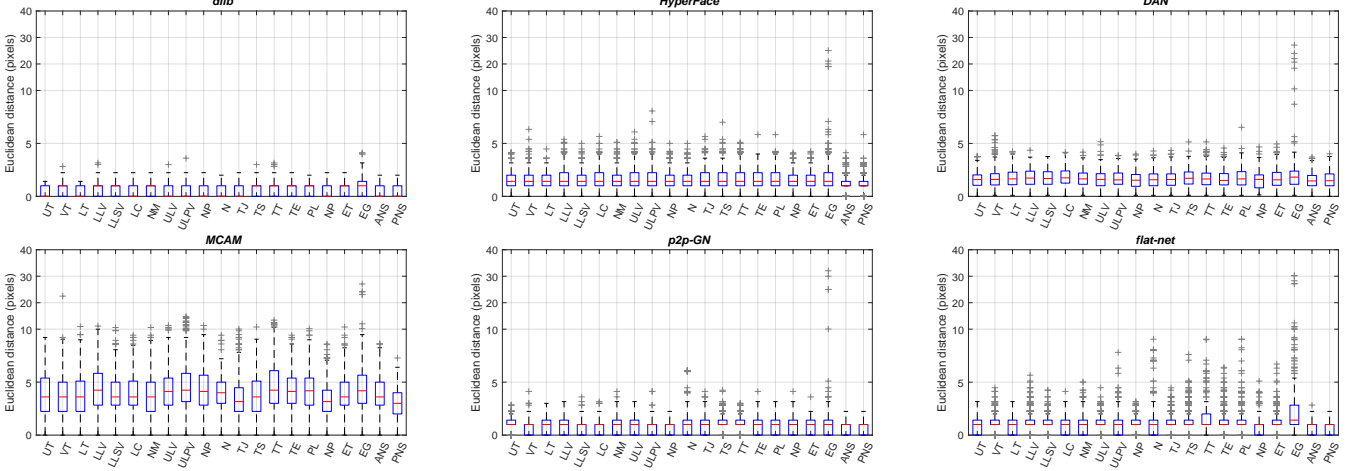


Fig. 6: Box plots of the Euclidean distance between the predicted and true landmark locations for the CV evaluation scheme.
Note the y-axis scale, linear in two steps to zoom in the 0-10 pixels range.

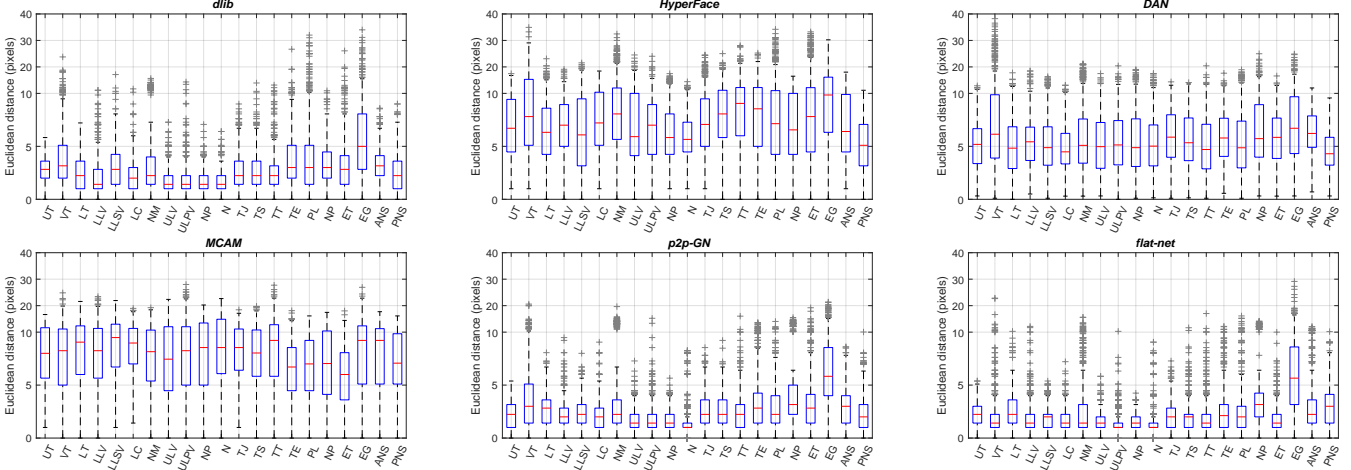


Fig. 7: Same as Fig. 6 but for the LoSo evaluation scheme.

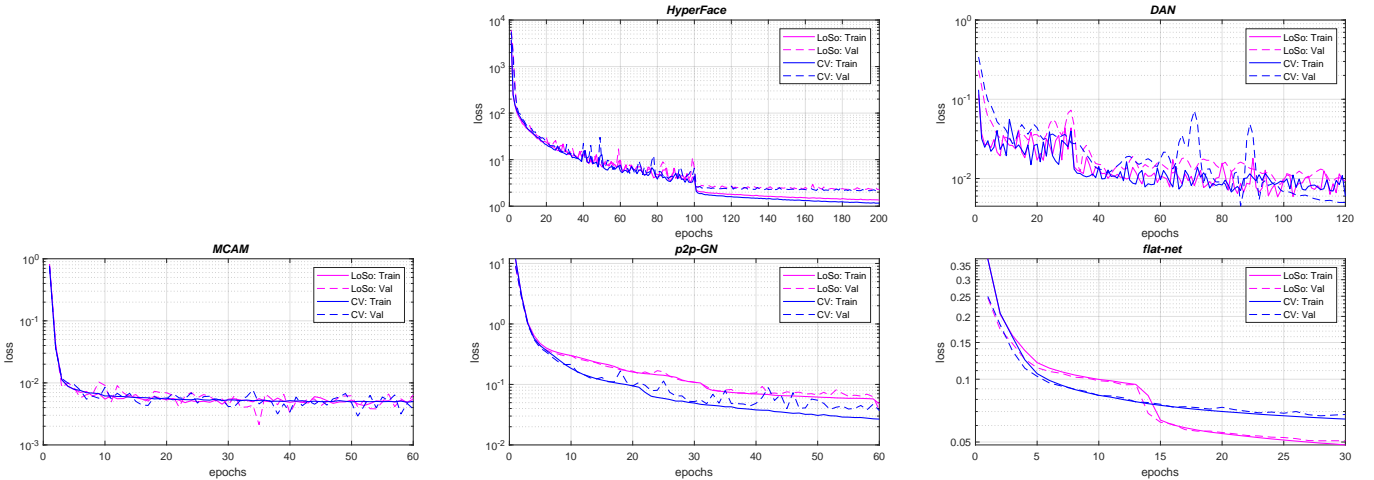


Fig. 8: (Color online) Learning curves, *i.e.* loss vs. epochs, for the training of the five networks of the study for the training (solid lines) and validation (dashed lines) data for the CV (blue lines) and LoSo (red lines) schemes.

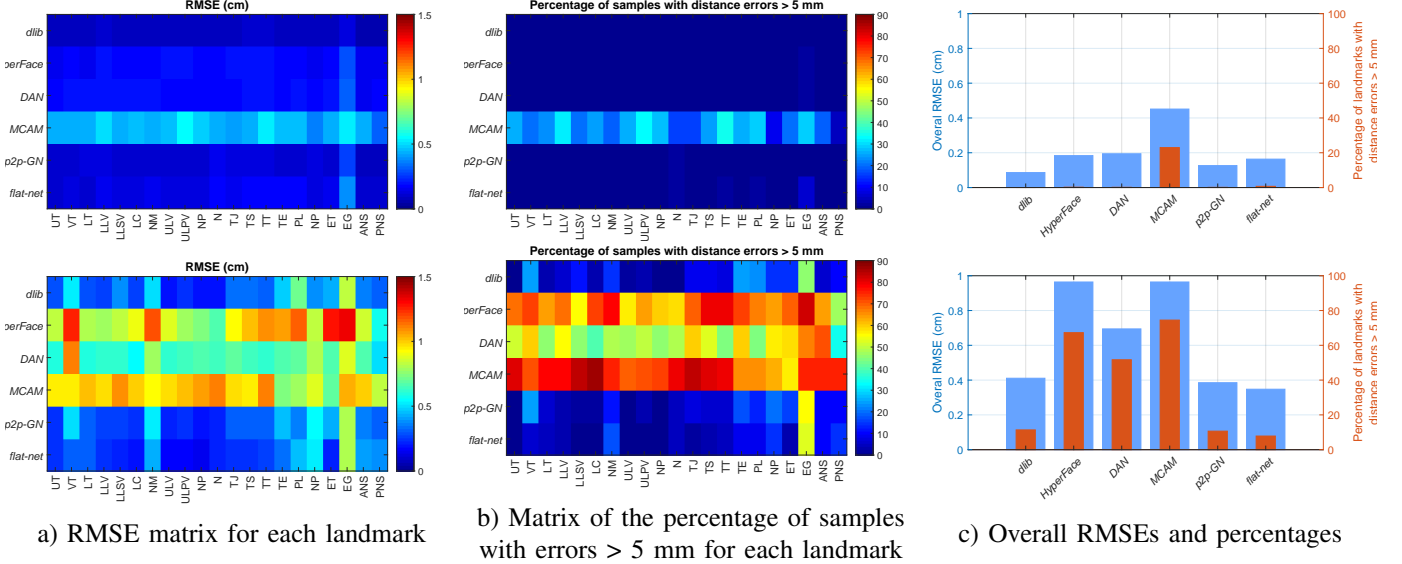


Fig. 9: (Color online) RMSE and percentage of samples with errors higher than 5 mm for the six methods of the study for the CV scheme (top) and the LoSo scheme (bottom).

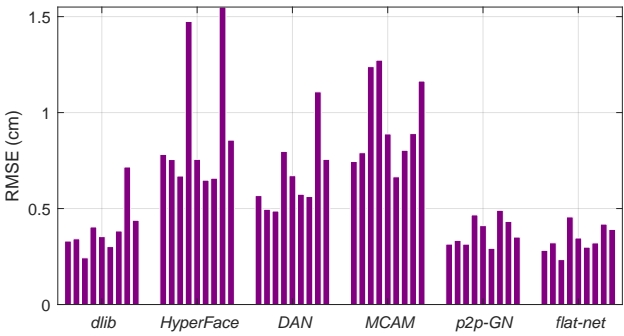


Fig. 10: Bar plots of the overall RMSEs per tested subject in LoSo scheme for the 6 methods of the study.

methods of the study is reported in Table II. Note that the storage space is reported for information but does not play in our eyes a critical role. Moreover, it depends on the data format and of the extent of the meta-data. In overall, the best results in LoSo scheme are reported for the *flat-net* method with a RMSE of 0.34 cm, slightly better than for the *dlib* and *p2p-GN* methods. Among these methods, the DL-based methods require significantly more training time and storage space. The *p2p-GN* method in particular has the largest number of weights to train and requires the largest space for storage. The *dlib* method is on the contrary rapidly trained, even on CPU, and requires the smallest space for storage.

The overall RMSEs per subject in LoSo scheme for the six methods of the study are displayed in Fig. 10. The *p2p-GN* and *flat-net* methods tend to show more homogeneous and lower errors across subjects, suggesting that they are the two more accurate and robust methods to predict the landmarks for new and unseen subjects. Some examples of practical results are reported in Table III.

B. Discussion

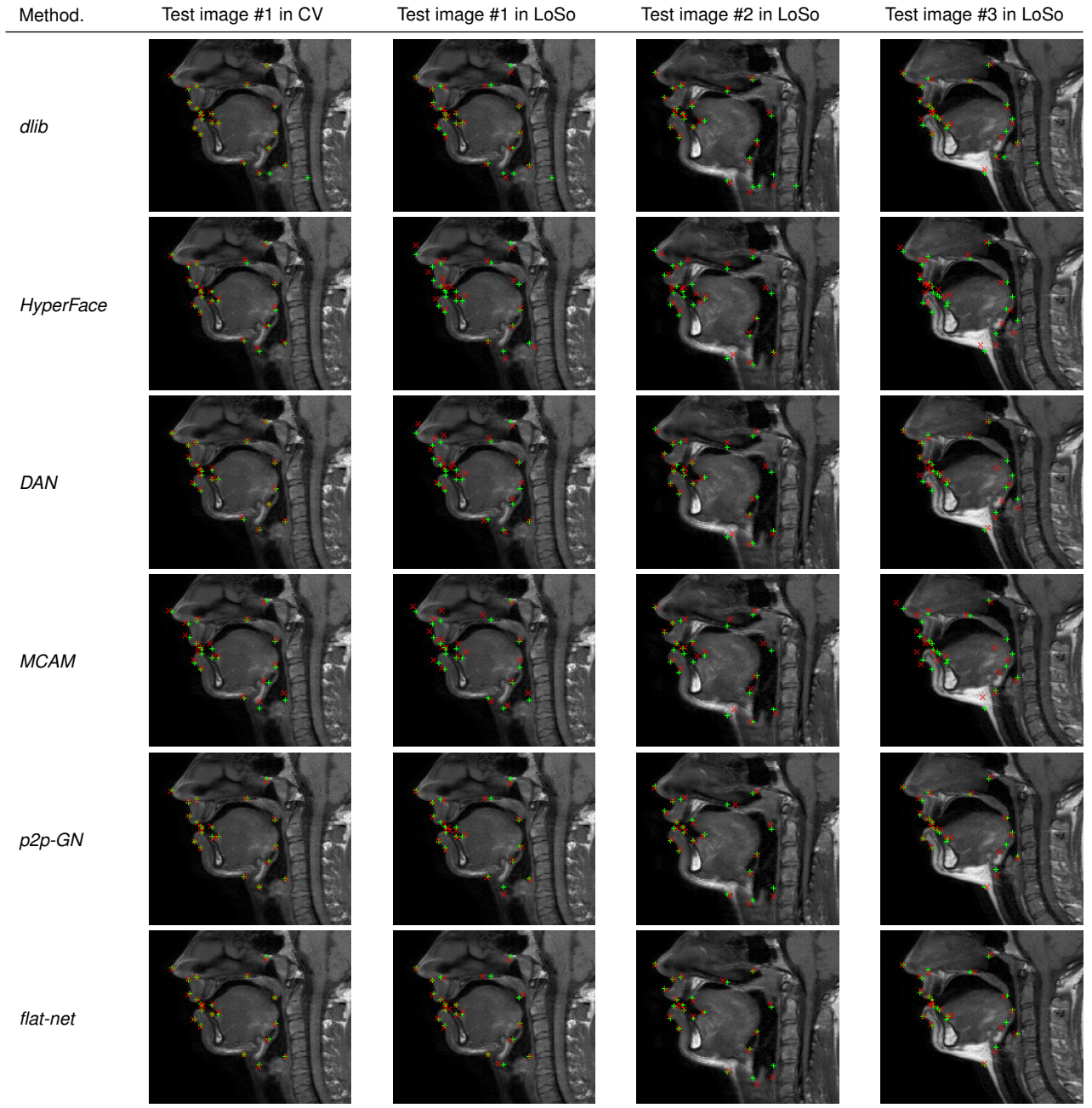
In general, the best results are achieved for the three methods *dlib*, *p2p-GN* and *flat-net*. Interestingly, it includes the only method not based on DL as well as the two methods specifically designed to solve the current problem. The good performance of the *dlib* method might be ascribed to the use of the boosting approach combined with the analysis of the input image in small regions by applying windows, possibly reducing the sensitivity to the variability of other regions of the image. The good performance of the *p2p-GN* and *flat-net* methods might be ascribed to the combination of the use of *heat-maps in channels* together with adapted networks. Indeed, although heat-maps are also somehow part of the *DAN* and *MCAM* methods, the design in channels as well as the use of networks able to output directly the heat-maps are successful. This approach leads to networks without fully connected layers, usually used to transform the feature maps into vectors of landmark locations in output. This may result in an architecture possibly less prone to error propagation, especially for such a limited dataset. In overall, the *flat-net* method, the only method entirely developed in this study, tends to be more robust and to present better performances. One could object that the better performance of the *flat-net* network come simply from its hyper-parameters optimized for the current problem. The results obtained in the CV evaluation scheme suggest however that all six methods – except the *MCAM* method to a certain extent – can perform the task with success, discarding this objection. These results support the approach using *heat-maps in channels* and networks without fully connects layers to localize landmarks of the vocal tract on MRI data.

Regarding the localization of the landmarks, the overall RMSEs in LoSo scheme for the three best methods identified above and for a subset of 13 out of 21 landmarks are displayed in Fig. 11: the 11 landmarks mentioned in the section II-B

TABLE II: Summary of the results and characteristics of the six methods of the study. The lowest occurrence for each line is written in blue.

Method	<i>MCAM</i>	<i>HyperFace</i>	<i>DAN</i>	<i>p2p-GN</i>	<i>flat-net</i>	<i>dlib</i>
RMSE in CV (cm)	0.45	0.18	0.19	0.12	0.16	0.08
RMSE in LoSo (cm)	0.96	0.96	0.69	0.38	0.34	0.41
Distance error in CV (pixels)	3.96 ± 3.86	1.49 ± 0.99	1.66 ± 0.84	0.89 ± 0.72	1.12 ± 1.29	0.59 ± 0.35
Distance error in LoSo (pixels)	8.47 ± 17.53	8.02 ± 24.92	5.81 ± 12.48	2.84 ± 6.16	2.39 ± 5.86	2.94 ± 7.54
Number of weights	14,500,480	35,168,006	$2 \times 23,104,092$	$7 \times 54,420,483$	$5 \times 2,958,533$	-
Number of epochs	60	200	2×120	7×60	5×30	-
Training time	150 (min)	50 (min)	2×130 min	7×55 (min)	5×88 (min)	55 (min) (cpu)
Storage space	210 MB	402 MB	2×280 MB	7×440 MB	5×34 MB	45 MB

TABLE III: (Color online) Three MRI images of different subjects and articulations zoomed in the region of the vocal tract and superimposed with the 21 ground truth (red crosses) and predicted (green crosses) landmarks for the six methods of the study in the LoSo scheme. The first image is also presented with results of the CV scheme.



and the landmarks N on the one hand and NM and EG on the other hand, presenting respectively the best and worst results. Note that these results are a zoom of the results presented in Fig. 9a. All these landmarks are more accurately located by the *flat-net* method, occasionally at the same precision than other methods. Except for NM, PL and EG, the RMSEs stay below 0.35 cm, a fairly good result considering the challenge associated with these landmarks and comparable to the overall RMSE achieved by the method. The landmarks UT and LT in particular, not visible on MRI and giving many problems in articulatory speech studies [35], are estimated with a respective accuracy of 0.25 cm and 0.3 cm for new speakers without additional *a priori* information. Similarly, the landmark TS, important for speech articulations and challenging to identify [36], is estimated with a precision of 0.25 cm. This emphasizes the robustness of the chosen approach through deep learning and the potential of these results for speech studies. The worst results are achieved for the landmarks NM, outside the range of the vocal tract, and EG and PL, in the larynx area. Although the larynx plays an important role in speech production, it remains at the margin of the vocal tract and does not play a central role in articulatory speech studies [3].

It should also be noted that some landmarks do not exhibit very salient characteristics, such as the junctions between the wet and dry vermillion of the lips (ULV and LLV) or the sublingual cavity posterior point (TS) when the tip of the tongue is in a low position. Similarly, some regions tend to be hardly interpretable in terms of anatomy, such the anterior part of the larynx associated with the landmark EG. Annotating manually their exact location on the images was a challenging task at the first point, questioning the quality of the ground-truth data and possibly explaining the lower accuracy achieved for EG. Furthermore, a detailed analysis of the results such as presented in Table III reveals that the location of some landmarks may appear occasionally more accurate in output of the presented methods than in the original so-called ground-truth. This is a well known effect of machine learning methods, and DL methods in particular, which tend to avoid encoding noise and outliers by means of regularization techniques [37], [38]. In general, a larger dataset labelled by several experts may limit the impact of the uncertainties in the ground-truth data and reinforce the robustness the DL methods and their resistance to noise.

The methods have been evaluated by means of two schemes, the CV and LoSo schemes. Strictly speaking, the most rigorous scheme would have been to leave both subject and articulation out, *i.e.* leave-one-subject-one-class-out (LoSoCo), to ensure that the network does not contain any information regarding the new tested image. In this scheme, all the articulations of one subject and one articulation of all subjects would be discarded in the training and the left articulation of the left subject would be tested. This would lead to $62 \times 9 = 558$ training sessions for each of the six methods. According to the times reported in Table II, it would take more than a year, making this evaluation unrealistic in practise. However, the challenge of the problem lies rather in the estimation of the landmark locations for a new speaker than for a new articulation. Indeed, the corpus of 62 articulations can be

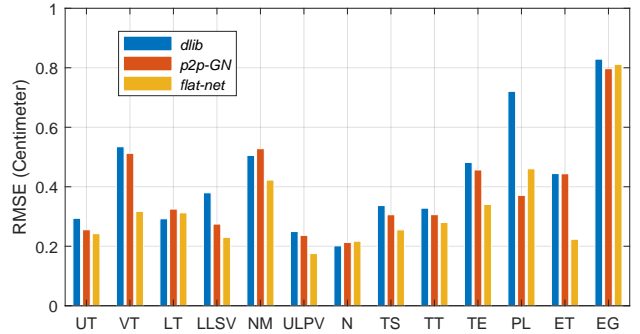


Fig. 11: (Color online) Bar plots of the overall RMSEs in LoSo scheme for the 3 methods *dlib*, *p2p-GN* and *flat-net* for a subset of 13 out of 21 landmarks.

considered large enough and representative of the French phonemic repertoire so that one articulation could fairly well be estimated from the 61 others [3]. For this reason, the LoSo scheme appears as a valid approximation to evaluate the methods on our problem.

In summary, the two methods introduced in this study outperform the state-of-the-art methods. It supports the description of landmarks in terms of *heat-maps in channels* and the generation of these heat-maps by means of DL networks without fully connected layers for such a variable and limited dataset. Future works may include the combination of successful features from the *dlib* method, showing very promising results, with DL approaches to create more robust methods, such as for instance the methods using deep forest networks [39], [40]. Furthermore, considering the recent rise of real-time MRI for speech production studies [12], the next steps will be to adapt this technique to real-time MRI data.

IV. CONCLUSIONS

The present paper described six methods to localize anatomical landmarks of the vocal tract area on MRI images. A dataset of midsagittal MRI from 9 speakers sustaining 62 articulations and annotated with the location of 21 landmarks has been considered for this purpose. Four methods taken from the literature have been considered, namely the *dlib* – the only non-deep learning approach, *Deep Alignment Network*, *HyperFace* and *Multi-Context Attention Model* methods. Two additional deep learning networks, the generator component of the *pix2pix* method and the *flat-net*, developed on purpose for this study, have also been considered to generate heat-maps in channels. These heat-maps describe each landmark location as a heat-map image stored in a channel of a single multi-channel image embedding all landmarks. The methods have been evaluated through two schemes, a randomized 10-fold scheme and a leave-one-speaker-out scheme, considered as more challenging. Experimental results confirm the deteriorated but more pertinent performance of the second scheme. More specifically, the *dlib*, *pix2pix* and *flat-net* methods outperformed the three other methods, leading to an overall Root Mean Square Error of 3.4 pixels/0.34 cm for the *flat-net* method, the most robust and accurate method. The *dlib* method

appeared interestingly as the less needy method regarding storage and computation resources. These results support the approach using heat-maps in channels combined with the adapted deep learning networks. Future works include the development of original methods combining the benefits of the *dlib* and *flat-net* methods and the adaptation of this approach to real-time MRI data.

ACKNOWLEDGEMENT

The authors are very grateful to P. Badin for providing the data, L. Lamalle recording them, and J.-A. Valdés Vargas and G. Ananthakrishnan for performing the majority of the initial landmark labelling. This research project is supported by the START-Program of the Faculty of Medicine, RWTH Aachen. Also, this work has been partially funded by the French ANR (grant ANR-08-EMER-001-02 'ARTIS').

REFERENCES

- [1] Harshman, R., Ladefoged, P. and Goldstein, L., 1977. Factor analysis of tongue shapes. *The Journal of the Acoustical Society of America*, 62(3), pp.693-707.
- [2] Beauremps, D., Badin, P. and Baily, G., 2001. Linear degrees of freedom in speech production: Analysis of cineradio-and labio-film data and articulatory-acoustic modeling. *The Journal of the Acoustical Society of America*, 109(5), pp.2165-2180.
- [3] Serrurier, A., Badin, P., Lamalle, L. and Neuschafer-Rube, C., 2019. Characterization of inter-speaker articulatory variability: A two-level multi-speaker modelling approach based on MRI data. *The Journal of the Acoustical Society of America*, 145(4), pp.2149-2170.
- [4] Yamasaki, R., Murano, E.Z., Gebrim, E., Hachiya, A., Montagnoli, A., Behlau, M. and Tsuji, D., 2017. Vocal tract adjustments of dysphonic and non-dysphonic women pre-and post-flexible resonance tube in water exercise: a quantitative MRI study. *Journal of Voice*, 31(4), pp.442-454.
- [5] Guzman, M., Miranda, G., Olavarria, C., Madrid, S., Muñoz, D., Leiva, M., Lopez, L. and Bortnem, C., 2017. Computerized tomography measures during and after artificial lengthening of the vocal tract in subjects with voice disorders. *Journal of voice*, 31(1), pp.124-e1.
- [6] Freitas, A.C., Wylezinska, M., Birch, M.J., Petersen, S.E. and Miquel, M.E., 2016. Comparison of Cartesian and non-Cartesian real-time MRI sequences at 1.5 T to assess velar motion and velopharyngeal closure during speech. *PloS one*, 11(4), p.e0153322.
- [7] De Alarcón, A., Prager, J., Rutter, M. and Wootten, C.T., 2019. Laryngeal and Tracheal Airway Disorders. In *Kendig's Disorders of the Respiratory Tract in Children* (pp. 1118-1124). Content Repository Only!.
- [8] Labrunie, M., Badin, P., Voit, D., Joseph, A.A., Frahm, J., Lamalle, L., Vilain, C. and Boán, L.J., 2018. Automatic segmentation of speech articulators from real-time midsagittal MRI based on supervised learning. *Speech Communication*, 99, pp.27-46.
- [9] Narayanan, S., Nayak, K., Lee, S., Sethy, A. and Byrd, D., 2004. An approach to real-time magnetic resonance imaging for speech production. *The Journal of the Acoustical Society of America*, 115(4), pp.1771-1776.
- [10] Story, B.H., 2005. Synergistic modes of vocal tract articulation for American English vowels. *The Journal of the Acoustical Society of America*, 118(6), pp.3834-3859.
- [11] Echternach, M., Burk, F., Burdumy, M., Traser, L. and Richter, B., 2016. Morphometric differences of vocal tract articulators in different loudness conditions in singing. *PloS one*, 11(4), p.e0153792.
- [12] Ramanarayanan, V., Tilsen, S., Proctor, M., Tügür, J., Goldstein, L., Nayak, K.S. and Narayanan, S., 2018. Analysis of speech production real-time MRI. *Computer Speech & Language*, 52, pp.1-22.
- [13] Zheng, Y., John, M., Liao, R., Nottling, A., Boese, J., Kempfert, J., Walther, T., Brockmann, G. and Comaniciu, D., 2012. Automatic aorta segmentation and valve landmark detection in C-arm CT for transcatheter aortic valve implantation. *IEEE transactions on medical imaging*, 31(12), pp.2307-2321.
- [14] Campbell, J.Q. and Petrella, A.J., 2015. An automated method for landmark identification and finite-element modeling of the lumbar spine. *IEEE Transactions on Biomedical Engineering*, 62(11), pp.2709-2716.
- [15] Zhang, J., Gao, Y., Wang, L., Tang, Z., Xia, J.J. and Shen, D., 2015. Automatic craniomaxillofacial landmark digitization via segmentation-guided partially-joint regression forest model and multiscale statistical features. *IEEE Transactions on Biomedical Engineering*, 63(9), pp.1820-1829.
- [16] De Zanet, S.I., Ciller, C., Rudolph, T., Maeder, P., Munier, F., Balmer, A., Cuadra, M.B. and Kowal, J.H., 2014. Landmark detection for fusion of fundus and MRI toward a patient-specific multimodal eye model. *IEEE transactions on biomedical engineering*, 62(2), pp.532-540.
- [17] Zhang, X., Tan, X., Gao, X., Wu, D., Zhou, X. and Fujita, H., 2018. Non-rigid registration of multi-phase liver CT data using fully automated landmark detection and TPS deformation. *Cluster Computing*, pp.1-15.
- [18] Liu, M., Zhang, J., Adeli, E. and Shen, D., 2018. Joint Classification and Regression via Deep Multi-Task Multi-Channel Learning for Alzheimer's Disease Diagnosis. *IEEE Transactions on Biomedical Engineering*, 66(5), pp.1195-1206.
- [19] Zhang, J., Gao, Y., Gao, Y., Munsell, B.C. and Shen, D., 2016. Detecting anatomical landmarks for fast Alzheimer's disease diagnosis. *IEEE transactions on medical imaging*, 35(12), pp.2524-2533.
- [20] Wu, Y. and Ji, Q., 2019. Facial landmark detection: A literature survey. *International Journal of Computer Vision*, 127(2), pp.115-142.
- [21] Sagonas, C., Tzimiropoulos, G., Zafeiriou, S. and Pantic, M., 2013. 300 faces in-the-wild challenge: The first facial landmark localization challenge. In *Proceedings of the IEEE International Conference on Computer Vision Workshops* (pp. 397-403).
- [22] Gong, W., Zhang, X., González, J., Sobral, A., Bouwmans, T., Tu, C. and Zahzah, E.H., 2016. Human pose estimation from monocular images: A comprehensive survey. *Sensors*, 16(12), p.1966.
- [23] Andriluka, M., Pishchulin, L., Gehler, P. and Schiele, B., 2014. 2d human pose estimation: New benchmark and state of the art analysis. In *Proceedings of the IEEE Conference on computer Vision and Pattern Recognition* (pp. 3686-3693).
- [24] Kazemi, V. and Sullivan, J., 2014. One millisecond face alignment with an ensemble of regression trees. In *Proceedings of the IEEE conference on computer vision and pattern recognition* (pp. 1867-1874).
- [25] Kowalski, M., Naruniec, J. and Trzciński, T., 2017. Deep alignment network: A convolutional neural network for robust face alignment. In *Proceedings of the IEEE Conference on Computer Vision and Pattern Recognition Workshops* (pp. 88-97).
- [26] Ranjan, R., Patel, V.M. and Chellappa, R., 2017. Hyperface: A deep multi-task learning framework for face detection, landmark localization, pose estimation, and gender recognition. *IEEE Transactions on Pattern Analysis and Machine Intelligence*, 41(1), pp.121-135.
- [27] Chu, X., Yang, W., Ouyang, W., Ma, C., Yuille, A.L. and Wang, X., 2017. Multi-context attention for human pose estimation. In *Proceedings of the IEEE Conference on Computer Vision and Pattern Recognition* (pp. 1831-1840).
- [28] Yang, J., Liu, Q. and Zhang, K., 2017. Stacked hourglass network for robust facial landmark localisation. In *Proceedings of the IEEE Conference on Computer Vision and Pattern Recognition Workshops* (pp. 79-87).
- [29] Isola, P., Zhu, J.Y., Zhou, T. and Efros, A.A., 2017. Image-to-image translation with conditional adversarial networks. In *Proceedings of the IEEE conference on computer vision and pattern recognition* (pp. 1125-1134).
- [30] Vargas, J.A.V., 2013. Adaptation of orofacial clones to the morphology and control strategies of target speakers for speech articulation (Doctoral dissertation).
- [31] Honari, S., Yosinski, J., Vincent, P. and Pal, C., 2016. Recombinator networks: Learning coarse-to-fine feature aggregation. In *Proceedings of the IEEE Conference on Computer Vision and Pattern Recognition* (pp. 5743-5752).
- [32] He, K., Zhang, X., Ren, S. and Sun, J., 2016. Deep residual learning for image recognition. In *Proceedings of the IEEE conference on computer vision and pattern recognition* (pp. 770-778).
- [33] Wang, T.C., Liu, M.Y., Zhu, J.Y., Tao, A., Kautz, J. and Catanzaro, B., 2018. High-resolution image synthesis and semantic manipulation with conditional gans. In *Proceedings of the IEEE conference on computer vision and pattern recognition* (pp. 8798-8807).
- [34] Bloice, M.D., Stocker, C. and Holzinger, A., 2017. Augmentor: an image augmentation library for machine learning. *arXiv preprint arXiv:1708.04680*.
- [35] Takemoto, H., Kitamura, T., Nishimoto, H. and Honda, K., 2004. A method of tooth superimposition on MRI data for accurate measurement of vocal tract shape and dimensions. *Acoustical science and technology*, 25(6), pp.468-474.
- [36] Ananthakrishnan, G., Badin, P., Vargas, J.A.V. and Engwall, O., 2010. Predicting unseen articulations from multi-speaker articulatory models. In

Eleventh Annual Conference of the International Speech Communication Association.

- [37] Zheng, Q., Yang, M., Yang, J., Zhang, Q. and Zhang, X., 2018. Improvement of generalization ability of deep CNN via implicit regularization in two-stage training process. *IEEE Access*, 6, pp.15844-15869.
- [38] Goodfellow, I., Bengio, Y. and Courville, A., 2016. Deep learning. MIT press.
- [39] Zhou, Z.H. and Feng, J., 2017. Deep Forest. *arXiv preprint arXiv:1702.08835*.
- [40] Orlando, J.I., Prokofyeva, E., del Fresno, M. and Blaschko, M.B., 2018. An ensemble deep learning based approach for red lesion detection in fundus images. *Computer methods and programs in biomedicine*, 153, pp.115-127.